Supporting Information

Synergistic Function of Bi and B in Interstitial Ternary Pd-Bi-B Alloy Nanocrystals for Highly Active and Durable Electrochemical Ethanol Oxidation

Poliraju Kalluru,‡[a] Ghufran Aulia Bin Azizar,‡[b] Respati K. Pramadewandaru,‡[c] Tae Gyun Kim,[a] Jieun Yu,[a] Dong Il Kang,[a] Jaehoon Jung,[a] Young Wook Lee*[d] and Jong Wook Hong*[b]

‡These authors contributed equally to this work

[a]P. Kalluru, T. G. Kim, J. Yu, D. I. Kang, J. Jung
Department of Chemistry, University of Ulsan, Ulsan 44776, South Korea

[b]G. A. B. Azizar, J. W. Hong
Department of Energy Engineering, Korea Institute of Energy Technology (KENTECH), Naju, 58330, South Korea
Email: jwhong@kentech.ac.kr (J.W.H)

[c]R. K. Pramadewandaru
Department of Materials and Metallurgical Engineering Sepuluh Nopember Institute of Technology Surabaya, East Java, Indonesia

[d]Y. W. Lee
Department of Education Chemistry and Research Institute of Natural Sciences, Gyeongsang National University, Jinju 52828, Republic of Korea
E-mail: lyw2020@gnu.ac.kr (Y.W.L)

Experimental

Nanocrystal separation

For of Pd_4Bi NCs, the mixture containing Pd_4Bi NCs was then centrifuged at 10,000 rpm for 10 min. Further, 3 to 4 times washed with a mixture of acetone and ethanol, centrifuged at 12,000 rpm for 10 min. For Pd_4Bi–B NCs, the product was washed three times with an ethanol, centrifuged at 8000 rpm for 7 min. Finally, the Pd4Bi–B NCs were dispersed in ethanol for further use.

Methods for ECSAs of catalysts

The electrochemical measurements of the double-layer capacitance (C_{dl}) and copper underpotential deposition (Cu-UPD) were performed via CV testing to assess the ECSA. CV scans were conducted at scan rates from 20 to 100 mV s^{-1} within a potential window free of faradaic processes (-0.85 V to 0.40 V vs. Hg/HgO). For the Cu-UPD experiments, an N_2 saturated electrolyte was used. Two different electrolyte compositions were employed such as 0.002 M Cu_2SO_4 + 0.05 M H_2SO_4 for acid condition and 0.010 M $CuSO_4$ + 1.0 M KOH for alkaline condition. In these experiments, the potential was held for 5 min at 0.3 V (vs. Ag/AgCl) for the acidic electrolyte and at -0.3 V (vs. Hg/HgO) for the alkaline electrolyte. The ECSA was calculated by subtracting the background CV responses, which were recorded in the N_2-saturated electrolyte.

Characterization

Transmission electron microscopy (TEM) images of the prepared catalysts were obtained by using a JEOL JEM-2100F respectively. ICP-OES measurement was conducted using a Spectroblue-ICP-OES (Ametek). X-ray diffraction (XRD) measurement was conducted on a Rigaku D/ MAX2500V/PC. X-ray photoelectron spectroscopy (XPS) measurements were

conducted by using a Thermo VG Scientific Sigma Probe spectrometer with Al Kα X-ray (1486.6 eV) as a light source. XPS data were calibrated using the C 1 s peak at 284.5 eV.

Density functional theory (DFT) calculation

The periodic DFT calculations were performed to investigate the influence of boron insertion into the interstitial octahedral sites of Bi-doped Pd nanocrystal (NC) on its electronic and geometric properties. We employed Perdew-Burke-Ernzerhof (PBE) functional[S1] implemented in the Vienna Ab-initio Simulation Package (VASP) code.[S2,S3] Grimme's D3 method[S4] was also utilized for dispersion corrections. The core electrons were replaced by projector-augmented wave (PAW) pseudopotentials,[S5] expanded in a basis set of plane waves up to a cutoff energy of 400 eV. Ionic (electronic) relaxations were performed until atomic forces (energies) were less than 0.01 eV/Å (10^{-7} eV). The 12×12×12 Γ-centered grids were used for the *k*-point sampling of the Brillouin zone. The optimized lattice constants of 3.88 (3.94) Å for Pd was obtained from PBE-D3 (PBE) calculations, which agrees well with the experimental value, 3.89 Å.[S6] Based on the atomic ratio of 1:4 between Bi and Pd estimated from the experimental results, we simply substituted one of four Pd atoms with a Bi atom in a conventional *fcc*-type Pd unit cell, which results in Bi:Pd = 1:3, to minimize the structural complexity due to atomic substitution in an approximated manner (Fig. S4). Two kinds of the octahedral (Oh) sites, i.e., (i) Oh-I site composed of six Pd atoms and (ii) Oh-II site composed of four Pd and two Bi atoms, are available for boron insertion. The insertion of boron into Oh-I site is more favorable than that into O_h-II site by 1.70 (1.65) eV of which the relative energy was obtained using PBE-D3 (PBE) calculations. Therefore, B-insertion into Oh-I site, i.e., Pd–Bi–B model I, was mainly utilized to investigate the influence of B on the electronic and geometric structures of Pd–Bi binary alloy NC (Fig. S4c). The Bi substitution followed by B insertion leads to the geometric expansion of pristine *fcc* Pd lattice (see Table S3), and

accordingly the volumes of Pd–Bi and Pd–Bi–B become larger than that of Pd lattice by 16.3% and 35.1%, respectively. The interlayer distance between (111) plane of optimized Pd–Bi and Pd–Bi–B models are 2.36 and 2.48 Å which are in good agreement with the experimental observation. The electronic structures of Pd, Pd–Bi, and Pd–Bi–B models were examined with the projected density of states (PDOS) (Fig. 4 in the main manuscript) and crystal orbital overlap population (COOP) analysis (Fig. S5). The COOP analysis was carried out using LOBSTER software.[S7] Furthermore, considering the simplicity of our model structures, both model I and II for Pd–Bi–B system were employed for elucidating the charge redistribution between inserted B atom and directly neighboring Pd and Bi atoms using the charge density difference plot (Fig. 4b) and the population analysis obtained with the density-derived electrostatic and chemical (DDEC) method [S8] (Table S4).

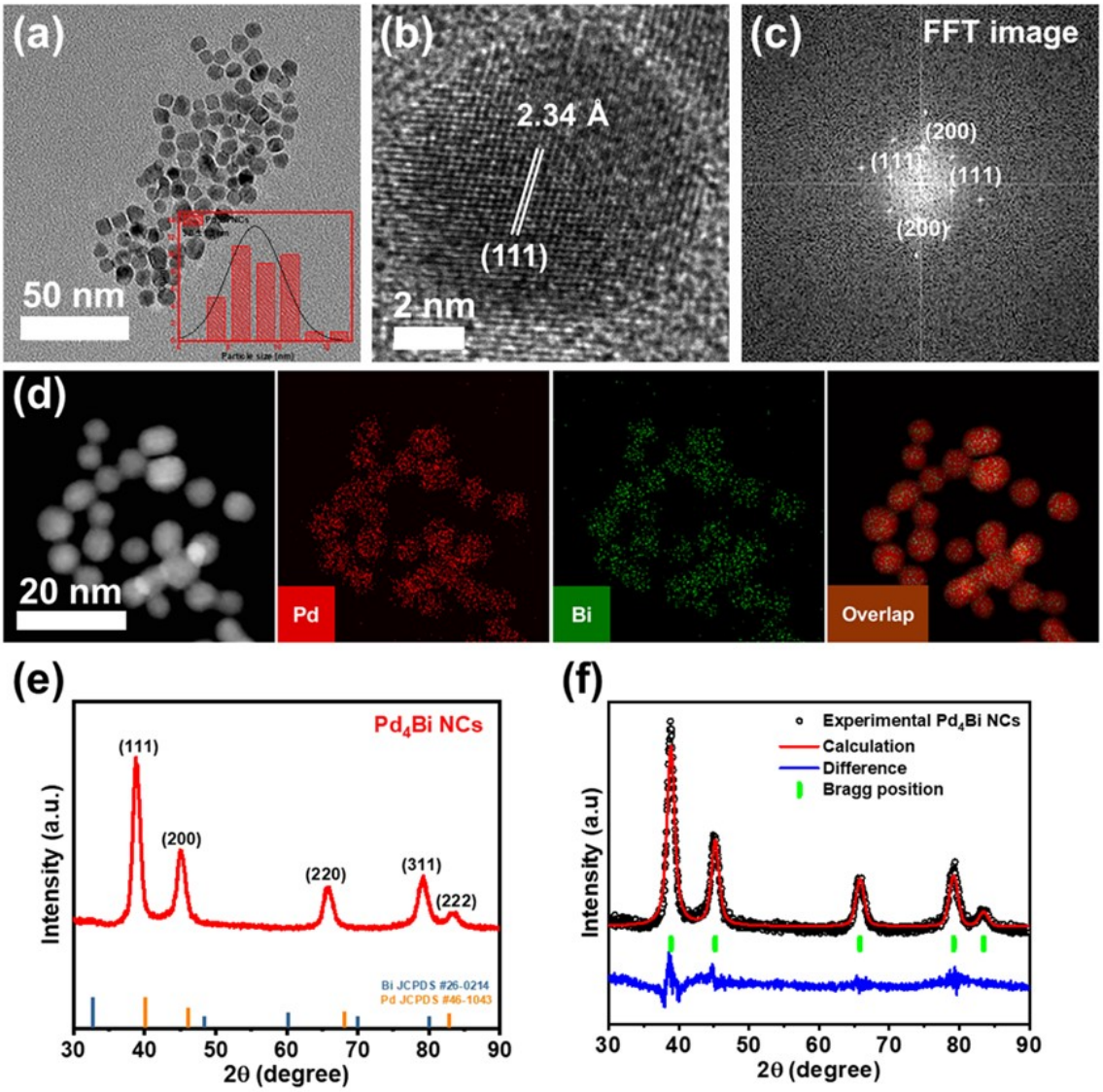

Fig. S1 (a) TEM image of Pd_4Bi NCs and particle size distribution (inset of Fig. S1a). (b) HRTEM image of Pd_4Bi NCs and (c) corresponding FFT pattern. (d) HAADF-STEM and corresponding EDS elemental mapping images of Pd_4Bi NCs. (e) XRD pattern and (f) Rietveld refinement of Pd_4Bi NCs.

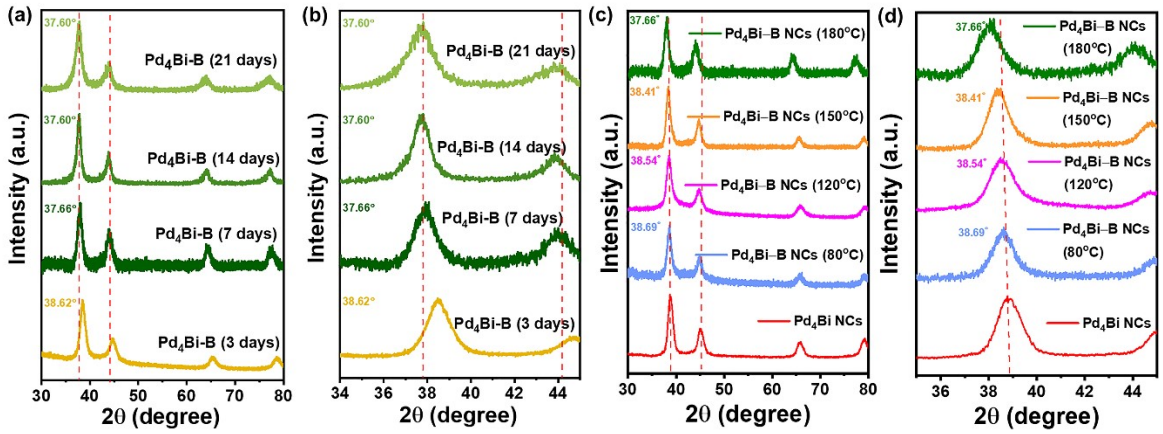

Fig. S2 XRD patterns of Pd_4Bi-B NCs with different (a) reaction times and (b) reaction temperatures.

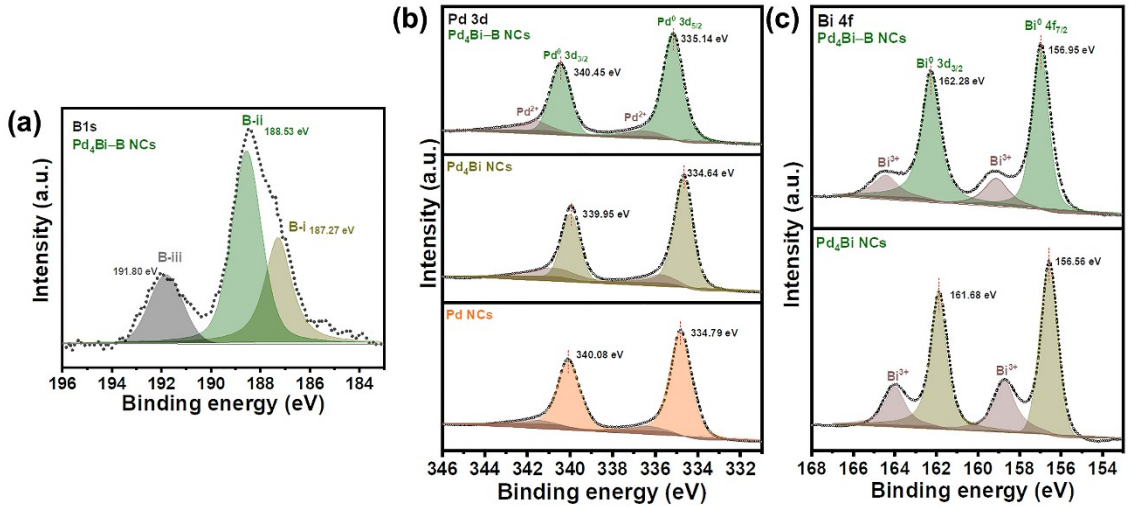

Fig. S3 (a) B 1s, (b) Pd 3d, and (c) Bi 4f core level XPS spectra of different catalysts.

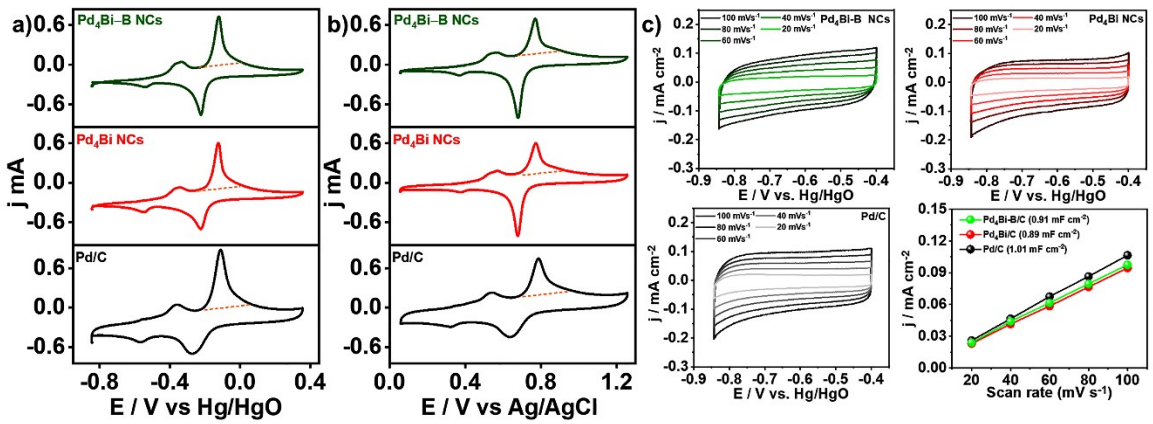

Fig. S4 Cu UPD curves for all catalysts in (a) 1.0 M KOH + 0.01 M $CuSO_4$ and (b) 1.0 M KOH + 0.01 M H_2SO_4. (c) C_{dl} plot in 1.0 M KOH with different scan rate.

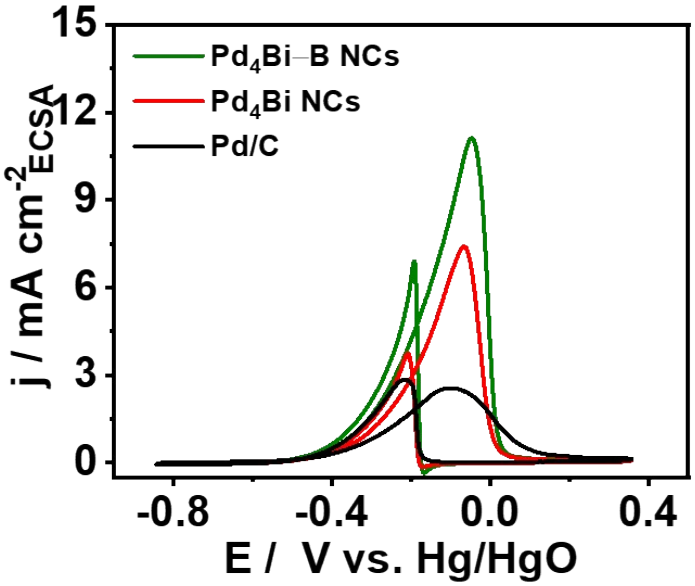

Fig. S5 Specific activity of different catalysts.

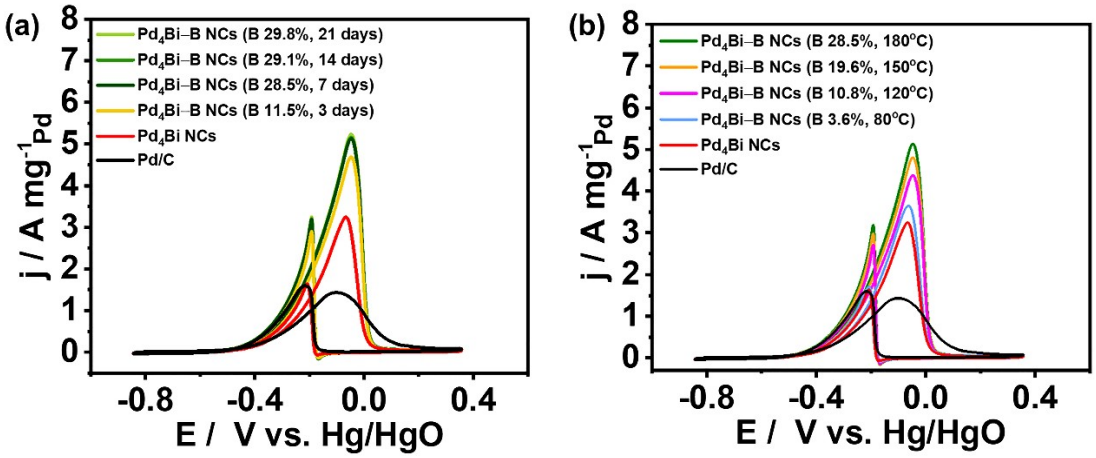

Fig. S6. CVs with Pd_4Bi-B NCs obtained from different (a) reaction times and (b) reaction temperatures.

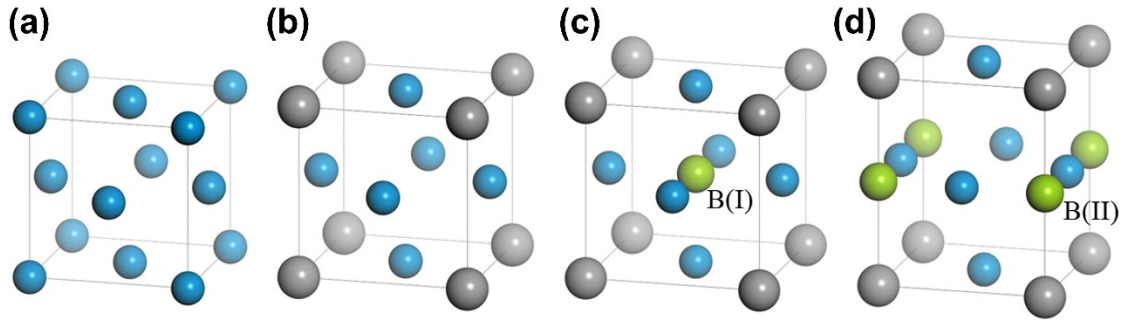

Fig. S7 Unit cell models for DFT calculations. (a) Pd, (b) Pd–Bi, (c) and (d) Pd–Bi–B models (Pd: blue, Bi: gray, B: green).

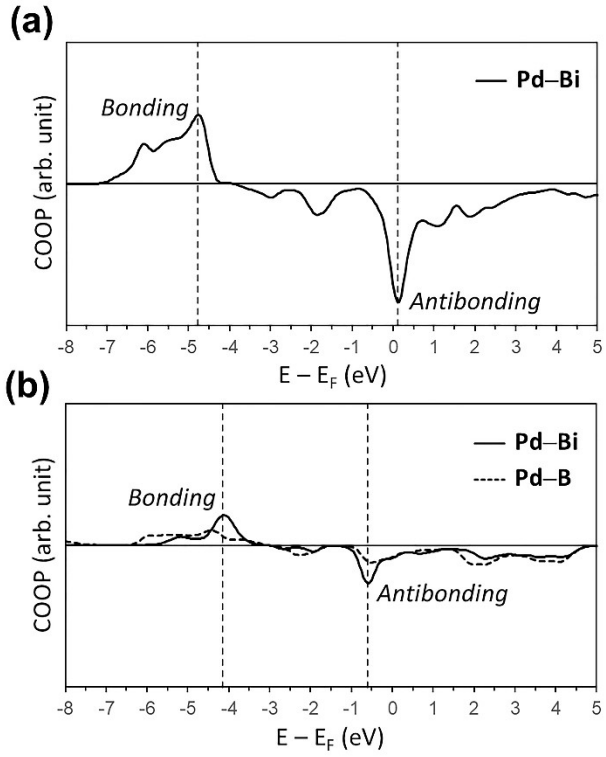

Fig. S8 The crystal orbital overlap population (COOP) for (a) Pd–Bi and (b) Pd–Bi–B models. The locations of bonding and anti-bonding states between Pd and Bi are indicated with dashed lines.

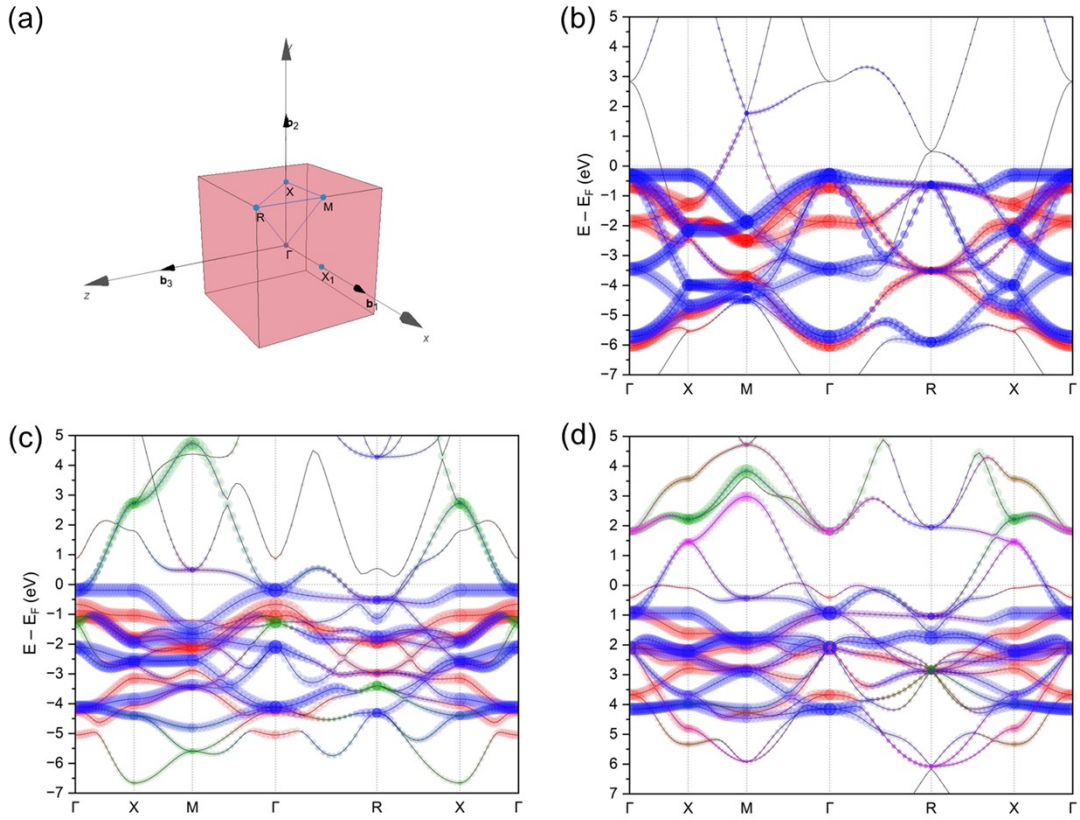

Fig. S9 (a) Electronic band path in Brillouin zone of Pd–Bi–B model, automatically generated in http://www.materialscloud.org/tools/seekpath. Electronic band diagrams for (b) Pd, (c) Pd–Bi, and (d) Pd–Bi–B models. The relative distributions of Pd 5d t_{2g}, Pd 5d e_g, Bi 2p, and B 2p states are represented with blue, red, green, and pink dots.

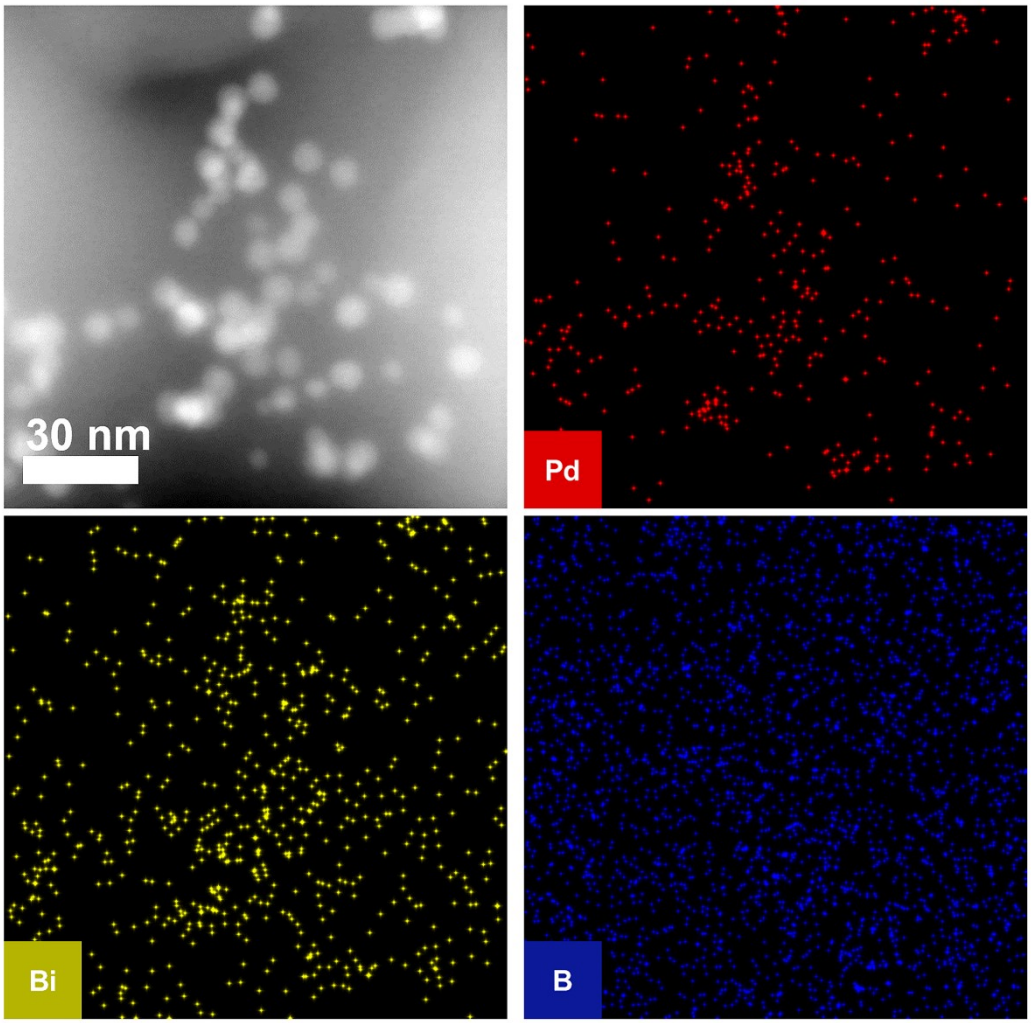

Fig. S10 HAADF-STEM and corresponding EDS elemental mapping images of Pd_4Bi–B NCs after the durability test (after 30000 cycles).

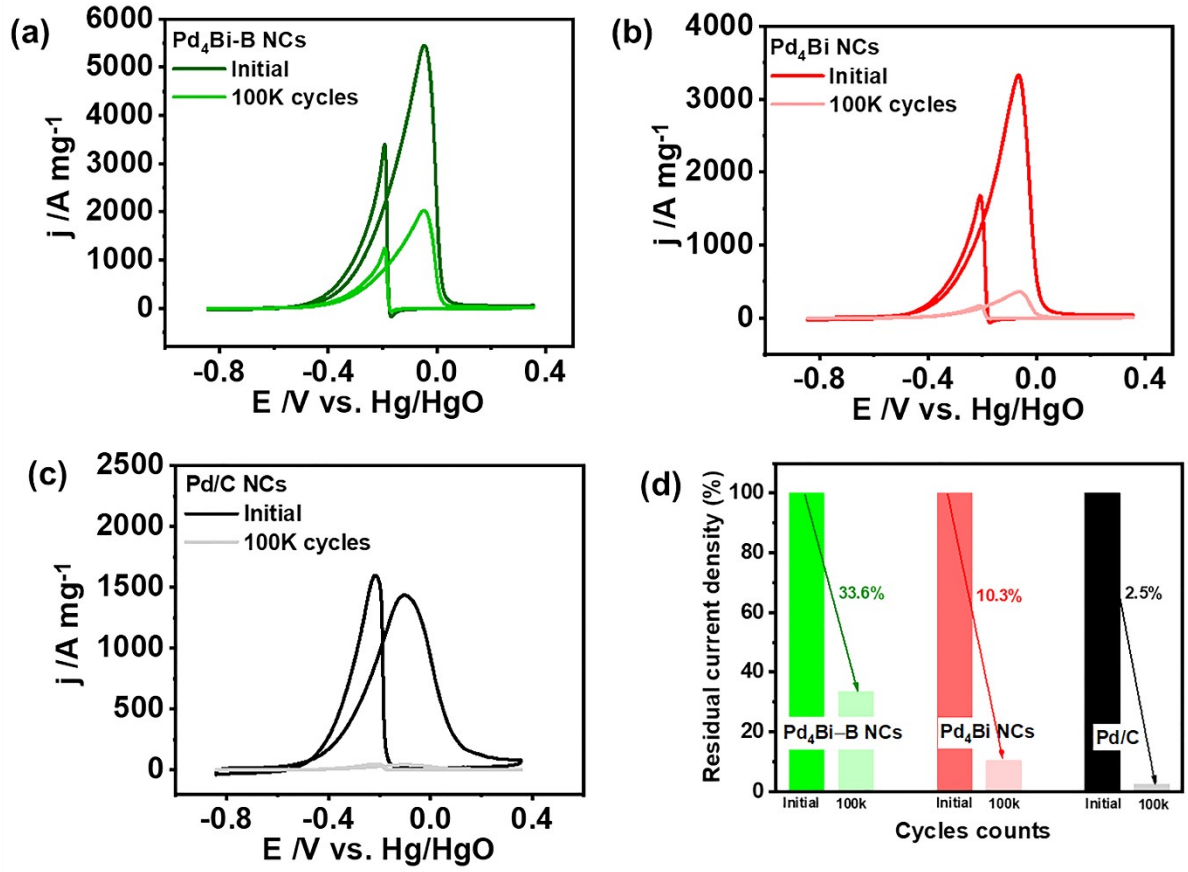

Fig. S11 (a-c) Accelerating durability test (ADT) for different catalysts under the scan rate of 50 mVs^{-1} in 1.0 M KOH + 1.0 M ethanol for 100,000 cycles. (d) Residual current density to the respective catalysts.

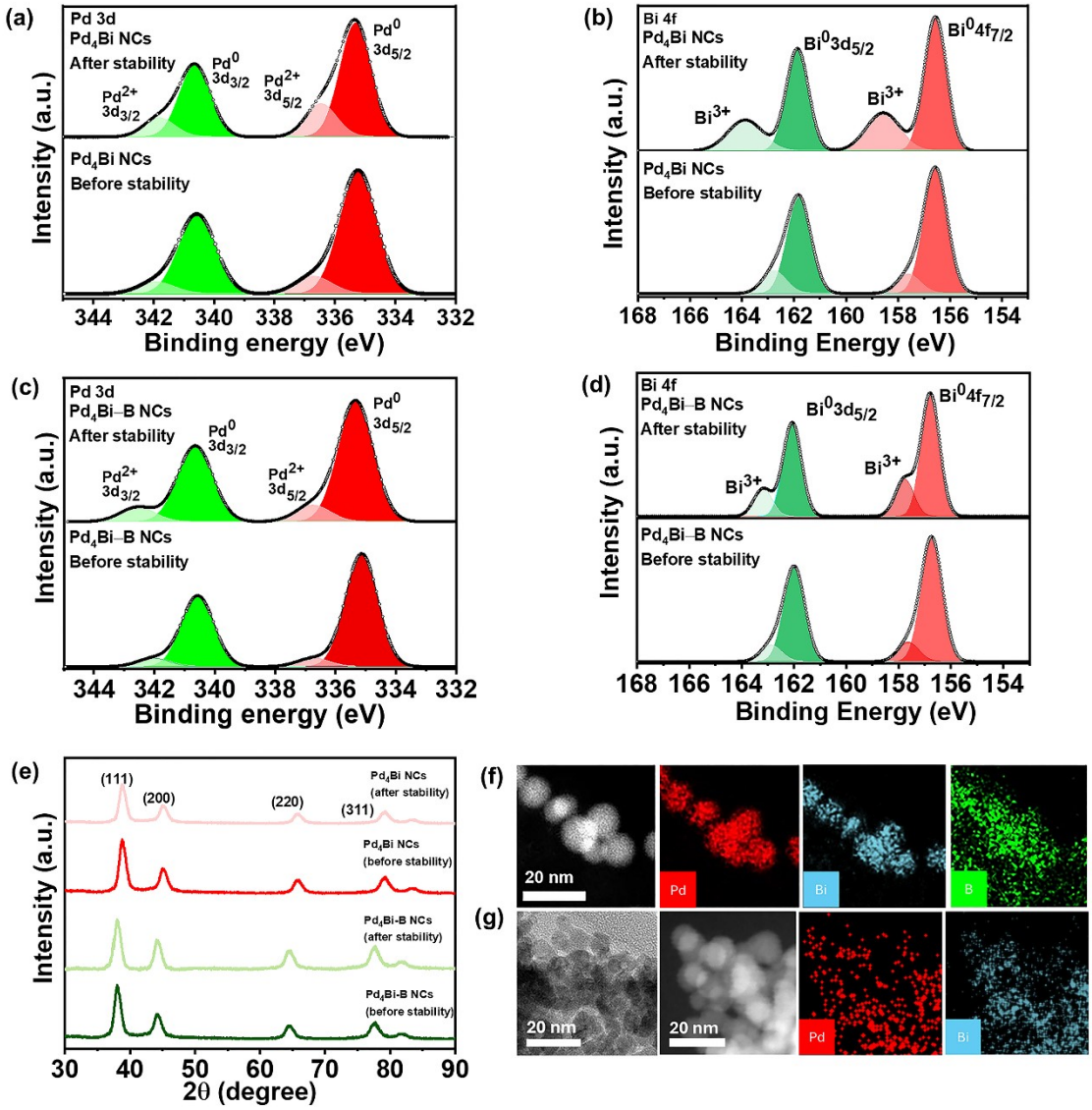

Fig. S12 (a-d) XPS spectra of Pd_4Bi and Pd_4Bi-B NCs before and after stability test. (a) Pd 3d and (b) Bi 4f core level XPS spectra of Pd_4Bi NCs. (c) Pd 3d and (d) Bi 4f core level XPS spectra of Pd_4Bi-B NCs. (e) XRD patterns of Pd_4Bi and Pd_4Bi-B NCs before and after stability test. TEM, HAADF-STEM, and corresponding EDS elemental mapping images of (f) Pd_4Bi-B and (g) Pd_4Bi NCs after the stability test.

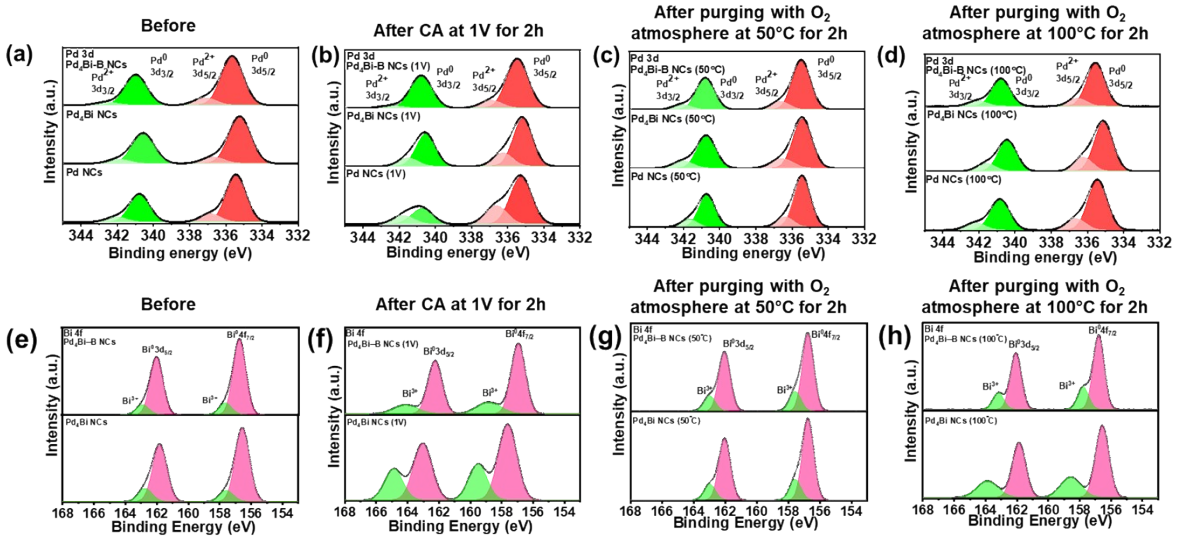

Fig. S13 (a-d) Pd 3d XPS spectra of Pd_4Bi-B, Pd_4Bi, and Pd NCs (a) before treatment, (b) after CA at 1 V_{RHE} for 2 h, (c) in an O_2 atmosphere at 50°C, and (d) in an O_2 atmosphere at 100°C. (e-h) Bi 4f XPS spectra of Pd_4Bi-B, Pd_4Bi, and Pd NCs (e) before treatment, (f) after CA at 1 V_{RHE} for 2 h, (g) in an O_2 atmosphere at 50°C, and (h) in an O_2 atmosphere at 100°C.

Table S1. The Pd/Bi/B atomic ratios with different reaction times and temperatures.

Catalyst	Pd (atomic%)	Bi (atomic%)	B (atomic%)
Pd_4Bi–B NCs (21 days)	**56.21**	**13.98**	**29.81**
Pd_4Bi–B NCs (14 days)	**56.78**	**14.10**	**29.12**
Pd_4Bi–B NCs (7 days)	**57.25**	**14.25**	**28.50**
Pd_4Bi–B NCs (3 days)	**71.15**	**17.35**	**11.50**
Pd_4Bi–B NCs (180°C)	**57.25**	**14.25**	**28.50**
Pd_4Bi–B NCs (150°C)	**65.29**	**15.09**	**19.62**

Pd_4Bi–B NCs (120°C)	**71.45**	**17.80**	**10.76**
Pd_4Bi–B NCs (80°C)	**75.87**	**20.55**	**3.58**
Pd_4Bi NCs	**80.10**	**19.90**	**-**

Table S2. The mass activities and specific activities of different catalysts in 1.0 M KOH + 1.0 M ethanol.

Catalyst	Mass Activity	Specific Activity
Pd_4Bi–B NCs	5240 mA mg^{-1}	11.13 mA cm^{-2}
Pd_4Bi NCs	3300 mA mg^{-1}	7.51 mA cm^{-2}
Pd/C	1320 mA mg^{-1}	2.61 mA cm^{-2}

Table S3. Lattice constant, interlayer distance between (111) planes [$d_{(111)}$], and d-band center for the conventional unit cells of Pd, Pd–Bi, Pd–Bi–B models, which were estimated using PBE-D3 (PBE) calculations. The energetically stable Pd-Bi-B model I was used to obtain numerical data.

	Pd	**Pd–Bi**	**Pd–Bi–B**
Lattice constant (Å)	3.88 (3.94)	4.08 (4.14)	4.29 (4.33)
$d_{(111)}$ (Å)	2.24 (2.28)	2.36 (2.39)	2.48 (2.50)
d-band center (eV)	–1.97 (–1.83)	–1.79 (–1.69)	–2.11 (–2.03)

Table S4. Net atomic charge (in *e*) obtained using density-derived electrostatic and chemical (DDEC) method. The asterisk star (*) indicates the charge transfer from the directly neighboring Pd and Bi atoms to B in Pd–Bi–B models.

	Pd–Bi	**Pd–Bi–B (model I)**	**Pd–Bi–B (model II)**
Pd	–0.024	0.141*	0.069*
			–0.053
Bi	0.072	0.061	0.285*
B		–0.486	–0.370

Table S5. Comparison of EOR activities of Pd_4Bi–B and Pd_4Bi NCs with previously reported catalysts.

Catalyst	Mass activity	References
Pd_4Bi–B NCs	**5240 mA mg^{-1}**	**This work**
Pd_4Bi NCs	**3300 mA mg^{-1}**	**This work**
$Pd_{14}Ag_1$ NP	243 mA mg^{-1}	76
WF-PdCu NSs	475 mA mg^{-1}	77
PdAgCu NWs	4640 mA mg^{-1}	78
PdPtCu NSs	2607 A mg^{-1}	79
PdBi-$Bi(OH)_3$	4460 mA mg^{-1}	80
PdCu@N-G	4300 mA mg^{-1}	81
PdBP MSs	3650 m A mg^{-1}	82
$Pd_{0.9}Sb_{0.1}$/PC	4244 mA mg^{-1}	83
CoP/RGO-Pd	4597 mA mg^{-1}	84
Pd_2Sn:P/C	5003 mA mg^{-1}	85
$Pd_{76}Ag_{24}$ WNWs	3480 mA mg^{-1}	86
TS-Pd/C	1846 mA mg^{-1}	87
PdAg/30CeO_2/C	4941 mA mg-1	88

Table S6. Comparison of EOR durability of Pd_4Bi–B and Pd_4Bi NCs with previously reported catalysts.

Catalyst	Mass activity	ADT result (residual current density / %)	References
Pd_4Bi–B NCs	**5240 mA mg^{-1}**	**30k cycles – 79.9%**	**This work**
PdS_x/C	170 mA mg^{-1}	3.6k cycles – 64.4 %	60
$Pd_{50}W_{27}Nb_{23}$/C	1560 mA mg^{-1}	3k cycles – 69.9 %	61
PdNi-HNPs-R/C	1200 mA mg^{-1}	1.5k cycles – 79.1 %	62
mPdNi/Ni NTs	1520 mA mg^{-1}	1k cycles – 82.1%	63
Pd_1Nb_1/C	850 mA mg^{-1}	1k cycles – 55.3 %	64
PdSn NCs	2700 mA mg^{-1}	0.5k cycles – 64.1 %	65
PdRhTe NTs	3400 mA mg^{-1}	0.5k cycles – 80.4 %	66
Pd-Au HNS	9100 mA mg^{-1}	2k cycles – 89.1 %	67
Pd-$CeO_{2\text{-}NR}$/C	1130 mA mg^{-1}	2k cycles – 61.2 %	68
Pd NPs@Ni SAC	1093 mA mg^{-1}	4.0k cycles - 90 %	69
PdB NWs	3390 mA mg^{-1}	10k cycles-74%	70
Pdene/$Ti_3C_2T_x$	7470 mA mg^{-1}	500 cycles – 94%	71
Pd-Pt alloy	3369 mA mg^{-1}	0.3 cycles – 71.2%	72
Pd-Sn/TiO_2	3381 mA mg^{-1}	0.3 cycles – 80%	73

PdMn-N_4/CNTs	3740 mA mg^{-1}	1000 cycles – 95%	74
Pd_{70}/$Ni(OH)_2$	1520 mA mg^{-1}	1000 cycles – 89.3%	75

References

S1 J. P. Perdew, K. Burke, M. Ernzerhof, *Phys. Rev. Lett.* 1996, **77**, 3865-3868.

S2 G. Kresse, J. Hafner, *Phys. Rev. B* 1993, **47**, 558-561.

S3 G. Kresse, J. Furthmüller, *Phys. Rev. B* 1996, **54**, 11169-11186.

S4 S. Grimme, J. Antony, S. Ehrlich, H. Krieg, *J. Chem. Phys.* 2010, **132**, 154104.

S5 G. Kresse, D. Joubert, *Phys. Rev. B* 1999, **59**, 1758-1775.

S6 J. W. Arblaster, Platin. *Met. Rev.* 2012, **56**, 181-189.

S7 R. Nelson, C. Ertual, J. George, V. Deringer, G. Hautier, R. Dronskowski, *J. Comput. Chem.* 2020, **41**, 1931-1940.

S8 T.A. Manz, D.S. Sholl, *J. Chem. Theory Comput.* 2012, **8**, 2844-2867